J. Fluid Mech. (1982), *vol.* 115, *pp.* 251–282
Printed in Great Britain

Measurement and prediction of mean velocity and turbulence structure in the near wake of an airfoil

By C. HAH AND B. LAKSHMINARAYANA
Department of Aerospace Engineering, The Pennsylvania State University, University Park, PA 16802, U.S.A.

(Received 1 October 1980)

An experimental investigation of the near wake of a thin airfoil at various incidence angles is reported in this paper. The airfoil (NACA 0012 basic thickness form) was located in a wind tunnel, and the wake structure was measured using hot-wire sensors. The measurements of mean-velocity, turbulence intensity and Reynolds-stress components across the wake at several distances downstream show the complex nature of the near wake and its asymmetrical behaviour. The asymmetry in the wake property, which is maintained up to a length of 1·5 chords downstream of the trailing edge of the blade, is dependent on the incidence angle of the inlet flow. The streamwise velocity defect in an asymmetric wake decays more slowly compared to that of a symmetric wake. The streamline curvature due to the blade loading has a substantial effect on the mean velocity profile as well as the turbulence structure. The numerical study of the same wake indicates that the existing turbulence closure models need some modification to account for the asymmetric characteristics of the wake.

1. Introduction

The study of the characteristics of the asymmetric near wake of an isolated airfoil has significant scientific and engineering applications. Most of the previous study in this area has been concerned with the far wake (e.g. cylinder) or the symmetric wake (as in the case of zero loading). The turbulence structure and mean velocity profiles of the asymmetric wake of streamlined bodies, such as airfoils, have been known to be different from that of the symmetric wake.

The objective of the present study is to measure and to predict the mean velocity and turbulence structure in the near wake of an isolated airfoil. Operation of the airfoil at different incidences provides the asymmetry in the wake, a case which is of extreme practical and scientific interest. The present experiment also provides scientific data for validating various turbulence models and numerical techniques, since this data includes the effect of simple streamline curvature, flow in the trailing-edge region, as well as the asymmetric nature of the wake.

Silverstein, Katzoff & Bullivant (1939) studied the turbulent wake of an airfoil experimentally. They measured the mean velocity profile at near and far wake, and provided empirical relationships for the wake decay. More systematic investigations of the mean velocity characteristics of the wake behind an isolated airfoil were carried out by Preston & Sweeting (1943) and Preston, Sweeting & Cox (1945). They observed similarity in velocity profiles and provided a general expression of the decay of velocity defect which is independent of the shape of the body or the loading on the body. This

expression is believed to be valid only in the far-wake region where the effect of physical characteristics of an airfoil and its loading are not important, and hence is devoid of all the flow history effects. None of the above investigators provided a detailed structure of mean velocity or turbulence characteristics. The only available data on the turbulence quantities in near and far wakes are those provided by Chevray & Kovasznay (1969). Unfortunately, they measured only three non-zero Reynolds stress components in the symmetric wake of a flat plate, and the data are inadequate in providing a valid test for various turbulence models and numerical flow prediction schemes.

No systematic measurement of mean velocity or turbulence quantities in the asymmetric wake has yet been reported. The effect of airfoil loading on the turbulence structure and the mean velocity characteristics has not yet been explored.

An experimental and numerical investigation of the asymmetric wake of an isolated airfoil with three different incidence angles (3°, 6°, 9°) at high Reynolds number (3×10^5 based on the chord length) is reported in this paper. In § 2, the physical nature of the airfoil wake is discussed. Detailed description of the governing equations, turbulence models employed and the numerical analysis are given in § 3. In § 4, the experimental set-up and measuring technique are discussed. The experimental results, interpretation and comparison with previous study are given in § 5. The experimentally measured quantities include mean velocity profiles and all the non-zero Reynolds stress components at various distances downstream of the airfoil trailing edge. In § 6, the numerical predictions with various turbulence models are presented, and the effect of the streamline curvature is also analysed.

2. Physical nature of the asymmetric wake of an airfoil

The wake of an isolated airfoil at non-zero incidence is asymmetric. The asymmetric nature in the wake is due to loading on the airfoil and the differing nature of boundary layers on the pressure and suction sides of the airfoil. The asymmetric nature of the wake disappears after about 1·5 chord downstream from the trailing edge of the airfoil. The asymmetric wake of an isolated airfoil has a different decay rate of mean velocity defect and turbulence quantities from those of a symmetric wake. This subject will be discussed further later.

The characteristics of an asymmetric wake can be classified and discussed in three categories, depending upon the flow evolution.

(*a*) *Very near wake:* In this region, the viscous sublayer on the airfoil is not completely mixed with the surrounding inertial sublayer. The molecular viscosity has a substantial effect on the flow evolution in the wake centre region. This region is confined to the trailing edge of the airfoil and the velocity defect is large.

(*b*) *Near wake:* In this region, the physical characteristics of the airfoil and aerodynamic loading on the airfoil have substantial effects on the evolution of the wake. For turbulent wake, the effect of molecular viscosity is negligible. The wake defect is of the same order as the mean velocity in this region.

(*c*) *Far wake:* In this region the wake structure is almost symmetric and the physical characteristics and aerodynamic loading have almost negligible effects on the development of the wake. The velocity defect is small and 'history effects' (such as airfoil shape or loading) have vanished.

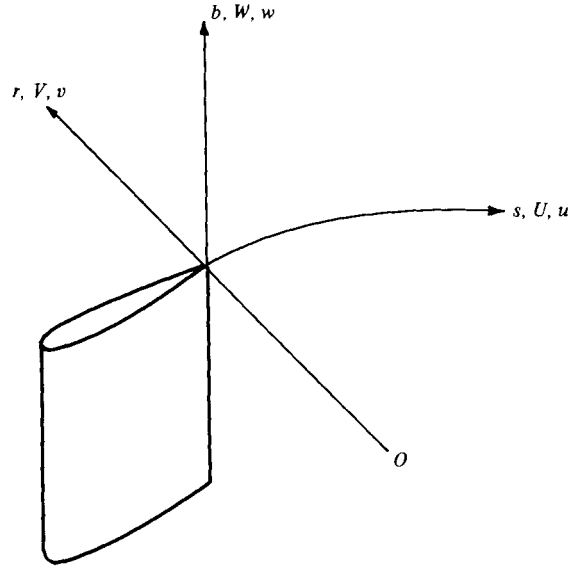

FIGURE 1. Co-ordinate system for the isolated airfoil wake.

3. Theoretical and numerical analysis of the airfoil wake

3.1. *Co-ordinate system and governing equations*

The curvilinear co-ordinates shown in figure 1 were chosen for the analysis of the curved turbulent wakes of an isolated airfoil. In this figure, r is the distance from the origin of the curvature, s is the streamwise distance from the trailing edge on the specified path and b is normal to s and r.

With this co-ordinate system, the actual streamline of the wake follows closely the s direction at the very-near- and the near-wake regions. Details of this co-ordinate system, matrix tensor, and Christoffel symbols are given by Hah (1980) and Hah & Lakshminarayana (1980*b*). The derived fundamental metric tensor and non-zero second kind of Christoffel symbols of this co-ordinate system are as follows:

$$(g_{ij}) = \begin{bmatrix} 1 & -\frac{s}{r} & 1 \\ -\frac{s}{r} & 1+\left(\frac{s}{r}\right)^2 & 0 \\ 0 & 0 & 1 \end{bmatrix}, \quad (g^{ij}) = \begin{bmatrix} 1+\left(\frac{s}{r}\right)^2 & \frac{s}{r} & 0 \\ \frac{s}{r} & 1 & 0 \\ 0 & 0 & 1 \end{bmatrix},$$

$$\Gamma^1_{11} = -\frac{s}{r^2}, \quad \Gamma^2_{11} = -\frac{1}{r}, \quad \Gamma^1_{12} = -\Gamma^2_{22} = \frac{s^2}{r^3}, \quad \Gamma^2_{21} = \frac{s}{r^2}, \quad \Gamma^1_{22} = -\frac{s^3}{r^4}. \tag{1}$$

The equations governing the steady incompressible flow for the chosen co-ordinate system are as presented below.

Continuity:

$$\frac{\partial U}{\partial s} + \frac{\partial V}{\partial r} = 0, \quad \frac{\partial u}{\partial s} + \frac{\partial v}{\partial r} = 0, \tag{2}$$

where U, V are mean contravariant velocity components in the streamwise (s) and

normal (r) directions, respectively (figure 1), and u, v are the corresponding fluctuating velocity components.

Momentum equations:

$$U\frac{\partial U}{\partial s}+V\frac{\partial U}{\partial r}+U^2\Gamma^1_{11}+V^2\Gamma^1_{22}+2UV\Gamma^1_{12}$$
$$=-\frac{1}{\rho}\left[\frac{s}{r}\frac{\partial p}{\partial r}+\left(1+\frac{s^2}{r^2}\right)\frac{\partial P}{\partial s}\right]-\frac{\partial\overline{uv}}{\partial r}-\frac{\partial\overline{u^2}}{\partial s}-\overline{u^2}\Gamma^1_{11}-\overline{uv}\Gamma^1_{12}-\overline{v^2}\Gamma^1_{12}$$
$$+\nu\left[\left(\frac{\partial^2 U}{\partial s^2}+\left(1+\frac{s^2}{r^2}\right)\frac{\partial^2 U}{\partial r^2}-2\frac{s}{r}\frac{\partial^2 U}{\partial s\,\partial r}\right]\right., \tag{3}$$

in which ν is kinematic viscosity;

$$U\frac{\partial V}{\partial s}+V\frac{\partial V}{\partial r}+U^2\Gamma^2_{11}+V^2\Gamma^2_{22}+2UV\Gamma^2_{12}$$
$$=-\frac{1}{\rho}\left(\frac{\partial P}{\partial r}+\frac{s}{r}\frac{\partial P}{\partial s}\right)-\frac{\partial\overline{uv}}{\partial s}-\frac{\partial\overline{v^2}}{\partial r}-\overline{u^2}\Gamma^2_{11}-\overline{v^2}\Gamma^2_{22}-\overline{uv}\Gamma^2_{12}$$
$$+\nu\left[\left(1+\frac{s^2}{r^2}\right)\frac{\partial^2 V}{\partial s^2}+\frac{\partial^2 V}{\partial r^2}+2\frac{s}{r}\frac{\partial^2 V}{\partial s\,\partial r}\right]. \tag{4}$$

3.2. *Theoretical considerations*

Mean velocity

The entire wake region of the flow field can be approximately divided into three regions, as explained earlier. Approximate analysis of the mean velocity defect, with its decay rate, based on the governing equations and suitable assumptions, is given below.

(*a*) *Very near wake:* The molecular viscosity is larger than the eddy viscosity in the wake centre region in this flow. Although this region is small ($su^*/\nu \leqslant 100$, u^* is frictional velocity at the wake centre and ν is molecular viscosity), the wake centre-line mean velocity recovers to about 60–70 per cent of the free-stream velocity in this region.

The U-momentum (3) on the wake centre line at the very near wake can be written as follows:

$$U\frac{\partial U}{\partial s}+U^2\Gamma^1_{11}=\nu\frac{\partial^2 U}{\partial r^2}+D_p, \tag{5}$$

where $D_p=-\rho^{-1}(1+s^2/r^2)\,\partial P/\partial s$ and is assumed to be constant at the very near wake. The turbulence terms are neglected because the molecular viscosity governs the fluid motion in this flow region.

From the linear velocity distribution in the viscous sublayer,

$$\frac{U}{u^*}=Y_+. \tag{6}$$

The thickness of the viscous sublayer is

$$Y_+\simeq 5. \tag{7}$$

Then

$$\nu\frac{\partial^2 U}{\partial r^2}=\frac{1}{5}\frac{u^3_*}{\nu}. \tag{8}$$

From (5) and (8),

$$\frac{d}{ds}U^2-2\frac{s}{r^2}U^2=\frac{2}{5}\frac{u^3_*}{\nu}+2D_p, \tag{9}$$

and

$$\frac{U_c}{u_*} = \left(\frac{2}{5}\right)^{\frac{1}{2}} \left(\frac{u_* s}{\nu} + 5 D_p s u_*^2\right)^{\frac{1}{2}} \left(1 - \frac{2}{3}\frac{s^2}{r_c^2}\right)^{\frac{1}{2}}, \tag{10}$$

where r_c and U_c are the radius of the streamline curvature and velocity at the wake centre line, respectively. This equation represents the variation of the wake centre-line velocity at the very near wake and will be compared with the experimental data later.

(*b*) *Near wake:* The near wake is still transitional flow whose evolution is not slow. After the very near wake, the viscous sublayer is mostly mixed in with the neighbouring inertial sublayer. Therefore, the molecular diffusion is much less than the turbulent diffusion. For this region, Alber (1979) derived a similarity solution for the symmetric wake of a flat plate. His expression for the wake centre-line velocity is given by

$$\frac{U_c}{u_*} = \frac{1}{\kappa}(\ln g - \gamma) + B, \tag{11}$$

where $g(\ln g - 1) = \kappa^2(su^*/\nu)$ and κ, γ, B are constants.

The actual curve for this wake region is very similar to

$$\frac{U_c}{u_*} = \frac{1}{\kappa'} \ln \frac{su^*}{\nu} + B', \tag{12}$$

where κ' and B' are constants. This expression is the law of the wall and wake derived by Coles (1956) for a boundary layer.

For the asymmetric wake with streamline curvature, various assumptions used in the derivation of (11) are not valid. However, equation (11) is considered to be valid when the curvature effect is mild. The experimental data will be compared with (12) in § 5.

(*c*) *Far wake:* Schlichting (1968) obtained the following analytical solution for the turbulent wake of a body at far-downstream locations using the mixing-length concept:

$$\frac{U_d}{U_\infty} = \frac{\sqrt{10}}{18\beta}\left(\frac{s}{C_d d}\right)^{-\frac{1}{2}} \left\{1 - \left(\frac{y}{b}\right)^{\frac{3}{2}}\right\}^2, \tag{13}$$

where $U_d = U_\infty - U$, β is a constant, C_d is the section drag coefficient, d is the maximum thickness of the body and b is the local wake width. The above analytical solution is valid when $U_d \ll U_\infty$. Since the asymmetric wake becomes symmetric far downstream, the above solution is also valid for a wake which is asymmetric initially.

Turbulence quantities

The transport equation of turbulent kinetic energy can be derived from the momentum equation of fluctuating velocity components, as follows:

$$U^j k_{,j} = -(\overline{ku^j})_{,j} - \overline{2u^i P_{,i}}/\rho - \overline{u^i u^j} U_{i,j} - \overline{u^l u^j} U_{l,j} + \nu g^{lj} g^{il} (\overline{u_l u}_{i,lj} + \overline{u_i u}_{l,lj}), \tag{14}$$

where k is turbulence kinetic energy. In the present co-ordinate system, the production term can be written as

$$\begin{aligned} -\overline{u^i u^j} U_{i,j} - \overline{u^l u^j} U_{l,j} = &-\overline{u^2}\left(\frac{\partial U}{\partial s} + U^2\frac{s}{r^2} + V\frac{s^2}{r^3}\right) - \overline{v^2}\left(\frac{\partial V}{\partial r} + U\frac{s}{r^2} - V\frac{s^2}{r^3}\right) \\ &- \overline{uv}\left(\frac{\partial U}{\partial r} + \frac{\partial V}{\partial s} - \frac{U}{r} + U\frac{s^2}{r^3} + V\frac{s}{r^2} - V\frac{s^3}{r^4}\right). \end{aligned} \tag{15}$$

The following eddy viscosity is introduced for the simplification of (15):

$$-\overline{u^i u^j} = \nu_{\text{eff}}(U^i_{,j} + U^j_{,i}) - \tfrac{2}{3}kg^{ij}, \tag{16}$$

where ν_{eff} is effective eddy viscosity and g^{ij} is the fundamental metric tensor. Neglecting higher-order curvature terms, the production term can be written as follows:

$$-\overline{u^i u^j}U_{i,j} - \overline{u^j u^j}U_{i,j} = \nu_{\text{eff}}\left[2\left(\frac{\partial U}{\partial s}\right)^2 + 2\left(\frac{\partial V}{\partial r}\right)^2 + \left(\frac{\partial U}{\partial r}\right)^2 + \left(\frac{\partial V}{\partial s}\right)^2 + 2\frac{\partial U}{\partial r}\frac{\partial V}{\partial s} - \frac{U}{r}\frac{\partial V}{\partial s} - \frac{U}{r}\frac{\partial U}{\partial r}\right]. \tag{17}$$

This expression can be further simplified for the thin wake of an airfoil at near and far wake,

$$-\overline{u^i u^j}U_{i,j} - \overline{u^k u^j}U_{k,j} = \nu_{\text{eff}}\left[\left(\frac{\partial U}{\partial r}\right)^2 - \frac{U}{r}\frac{\partial U}{\partial r}\right]. \tag{18}$$

The second term represents the extra production of turbulent kinetic energy due to the streamline curvature. This extra production term increases the production of the turbulence kinetic energy when the angular momentum decreases in the direction of the curvature radius, and, conversely, the production of turbulence kinetic energy is decreased when the angular momentum increases in the direction of the curvature radius. The above effects of streamline curvature in the transport equation are consistent with the comprehensive analysis of the curvature effects presented by Bradshaw (1973).

3.3. *The numerical prediction of the airfoil wake*

The wake of an isolated airfoil is predicted by the numerical analysis of the exact equations, including several turbulence models. A description of this analysis follows.

Turbulence closure model: Various turbulence closure models were compared for the performance of the streamline curvature effect by Hah & Lakshminarayana (1980*a*). The k–ϵ equation model and Reynolds-stress model employ the following modelled transport equation for the rate of turbulence kinetic energy dissipation:

$$U^i\frac{\partial \epsilon}{\partial x^i} = \frac{\partial}{\partial x^i}\left(\frac{\nu_{\text{eff}}}{\sigma_\epsilon}\frac{\partial \epsilon}{\partial x^i}\right) + S - C_{\epsilon 2}\frac{\epsilon^2}{k}, \tag{19}$$

where $\nu_{\text{eff}} = C_\mu k^2/\epsilon$, S is the source term, ϵ is the rate of energy dissipation and $C_{\epsilon 2}$, σ_ϵ are constants.

Most turbulent-flow calculations have been done with the following expression for the source term:

$$S = C_{\epsilon 1}\frac{\epsilon}{k}P, \tag{20}$$

where $P_{ij} = -\overline{u_i u_j}U_{i,j}$ is a Cartesian tensor. As discussed in §3.2, the production P increases as the flow field is destabilized due to the streamline curvature and, consequently, the level of ϵ also increases. The effective eddy viscosity is proportional to k^2/ϵ for the models. Therefore, the resulting turbulence transport is not well represented for the effect of streamline curvature (both the k and ϵ increase when the flow field is destabilized and, consequently, the quantity k^2/ϵ does not change much). To represent the curvature effect accurately, various forms of the source term in the

dissipation equation were suggested by Hah & Lakshminarayana (1980*a*). The following form of the source term is used for the present calculation:

$$S_{ij} = C_l \epsilon^2 k^{-3} (\overline{u^i u^j} - \tfrac{2}{3} k \delta_{ij}) (\overline{u^j u^i} - \tfrac{2}{3} k \delta_{ji}). \tag{21}$$

A modelled form of the transport equation of the turbulence kinetic energy was also employed, as follows:

$$U^i \frac{\partial k}{\partial x^i} = \frac{\partial}{\partial x^i} \left(\frac{\nu_{\text{eff}}}{\sigma_\kappa} \frac{\partial k}{\partial x^i} \right) + P - \epsilon, \tag{22}$$

where k is the turbulence kinetic energy and σ_κ is a constant.

The Reynolds stress components were calculated with the following transport equation of Reynolds stress:

$$0 = (1 + C_1) (-\overline{u_l u^j} U^i_{,l} - \overline{u_l u^i} U^j_{,l}) (1 - \gamma) - \tfrac{2}{3} g^{ij} \epsilon (1 - \gamma) - C_{\phi 1} \frac{\epsilon}{k} (\overline{u^i u^j} - \tfrac{2}{3} g^{ij} k). \tag{23}$$

This equation is a simplified form of the exact Reynolds stress equation. The combined effect of the diffusion and the convective terms are related to the production term through the variable C_1. γ and $C_{\phi 1}$ are constants.

With the known values of U, W, k, ϵ at each point in the flow field, the four non-zero Reynolds stress components can be estimated from (23). Therefore, equations (19), (22) and (23) form an algebraic Reynolds stress closure model.

Numerical scheme: The governing equations (2), (3) and (4), together with the turbulence closure equations (19), (22) and (23), were solved in elliptic form. The calculation domain extended from the trailing edge to 1·5 chords downstream and one chord length on either side of the airfoil in the transverse direction. The experimental data was used as the initial condition at the trailing edge. In the free stream, the turbulence level was specified as the free-stream turbulence value at the trailing edge. The outlet flow boundary conditions were based on the correlation given by (13) and the correlations for the turbulence quantities derived in § 5 (equations (27) and (28)). The governing equations were approximated with the finite-difference equations, with central differences for spacial derivatives. The resulting finite-difference equations were solved iteratively using a line S.O.R. For the universal constants in (19) and (22), the values used by Pope & Whitelaw (1976) were employed. The expression given in (21) was used for the source term of the energy dissipation equation and the value of C_l was 1·8. The detailed descriptions of the finite-difference equation, boundary conditions and numerical procedure are given by Hah (1980). The result of numerical calculations will be presented in § 5.

4. Experimental method and instrumentation

The hot-wire anemometry technique was used for the measurement of mean velocity and turbulence quantities. A two-sensor cross-wire probe with nearly equal resistance (5·64 and 5·70 Ω) and length-to-diameter ratio (l/D = 350) was used in these measurements. To measure all three turbulence intensity components and the resultant shear stress, the cross wire was first placed in the plane containing the streamwise direction and perpendicular to the spanwise directions. The cross wire was then rotated so as to make one wire parallel to the spanwise direction during these measurements (*b* direction in figure 1).

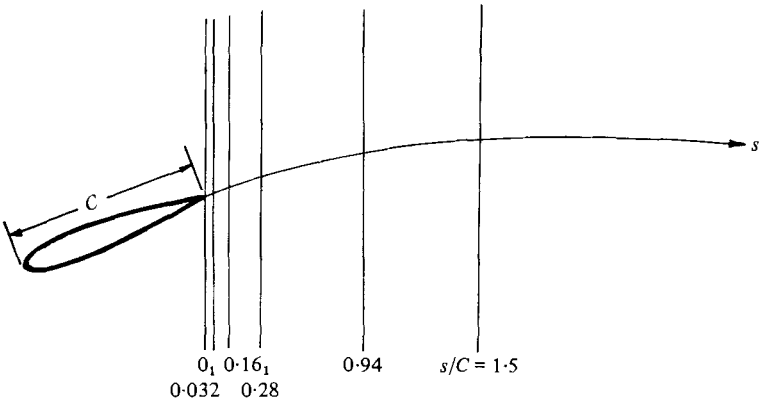

FIGURE 2. Measuring stations (airfoil is drawn to scale).

The output voltages from DISA 55M10 constant-temperature anemometers were digitized and statistically processed using the H.P. 2100-S computer system at the Department of Aerospace Engineering, The Pennsylvania State University. All the mean velocity and turbulence quantities were obtained through proper statistical averaging at the instantaneous velocity components. The hot-wire results were corrected for deviation from the cosine law. The details of the instrument set-up, the system of hot-wire equations, the error analysis and the statistical procedure are given by Hah (1980).

The measurements were performed in the subsonic wind tunnel. The wind tunnel has a test section of $1{\cdot}5 \times 1{\cdot}5 \times 2$ m, and the free-stream velocity in this section can be continuously raised up to 60 m s^{-1}. All the experiments were done at a free-stream velocity of 30 m s^{-1} and a turbulence level of free-stream of 0·2 %. The profile of the blade used in the experiment is the NACA-0012 basic thickness form with chord length of 0·2 m, spanwise length of 1·1 m. Details of this profile are given by Abbott & Doenhoff (1958), and the profile is shown plotted to scale in figure 2. The wake measurements were done at the centre of the span and the mean flow field was two-dimensional at the measuring stations. The incidence angle of the inlet flow varied systematically by 3°, 6° and 9°. The Reynolds number based on the chord length was $3{\cdot}8 \times 10^5$ throughout the experiment. The wake profile was measured at s/C = 0, 0·032, 0·16, 0·28, 0·94 and 1·5, as shown in figure 2. The traverse survey included about 25 stations across each wake.

5. Experimental results and comparison with predictions

Results of the comprehensive set of data acquired during this program is presented below. As mentioned earlier, such data is not available in the literature, and hence should serve as a useful set for validation of future analysis and numerical schemes.

5.1. *Mean velocity and related wake parameters*

As already mentioned, the mean velocity profiles and turbulence quantities were measured across the wake at several streamwise distances for three incidence angles. Plots of the mean velocity profiles are shown in figures 3(*a*, *b*, *c*), where $n = r - r_c$ and r_c is the radius of curvature at the wake centre and negative values of n indicate the

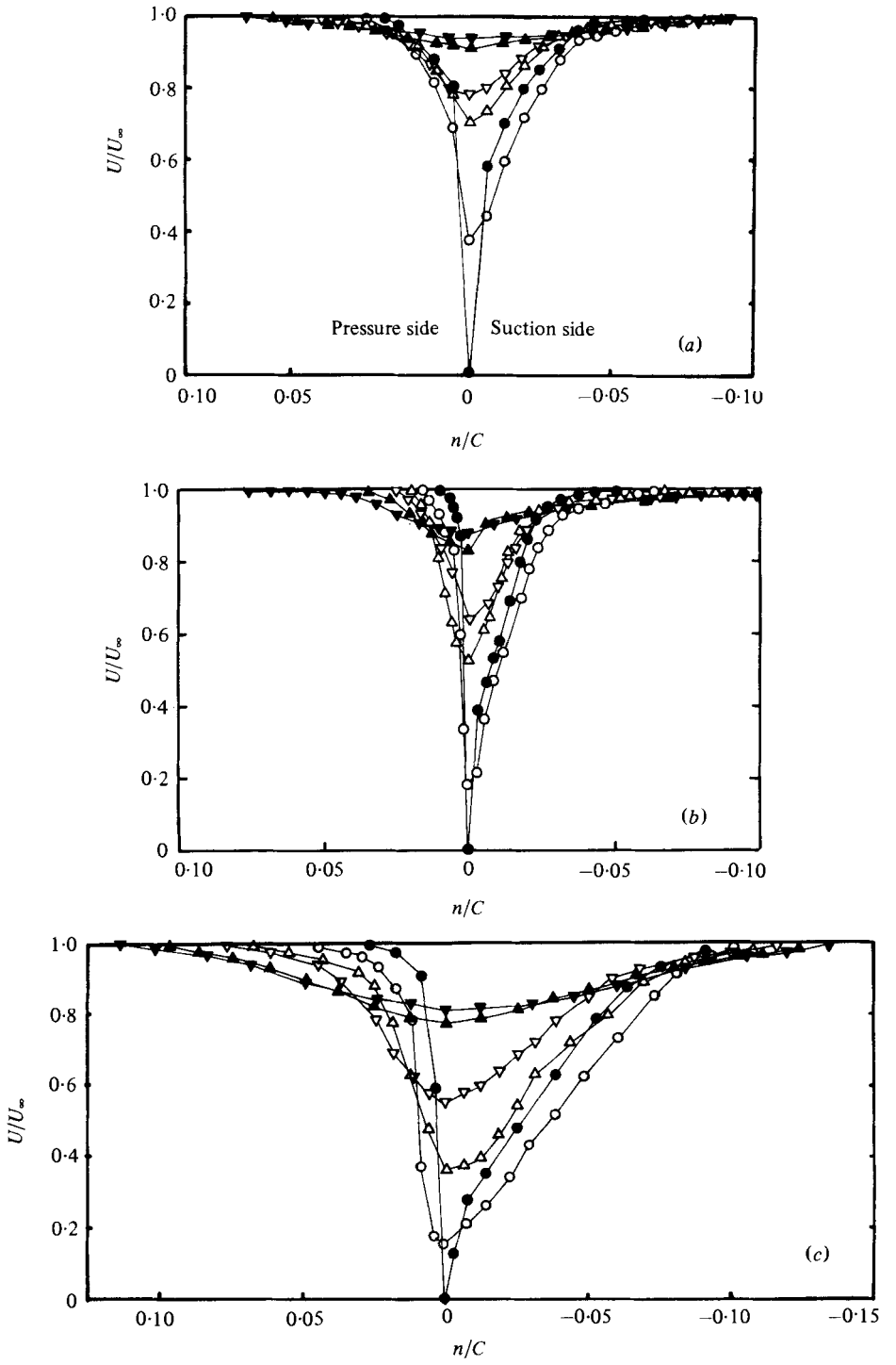

FIGURE 3. Streamwise velocity profile at (*a*) 3°, (*b*) 6° and (*c*) 9°. ●, $s/C = 0$; ○, $s/C = 0{\cdot}032$; △, $s/C = 0{\cdot}16$; ▽, $s/C = 0{\cdot}28$; ▲, $s/C = 0{\cdot}94$; ▼, $s/C = 1{\cdot}5$. (See figures 1 and 2 for notation.)

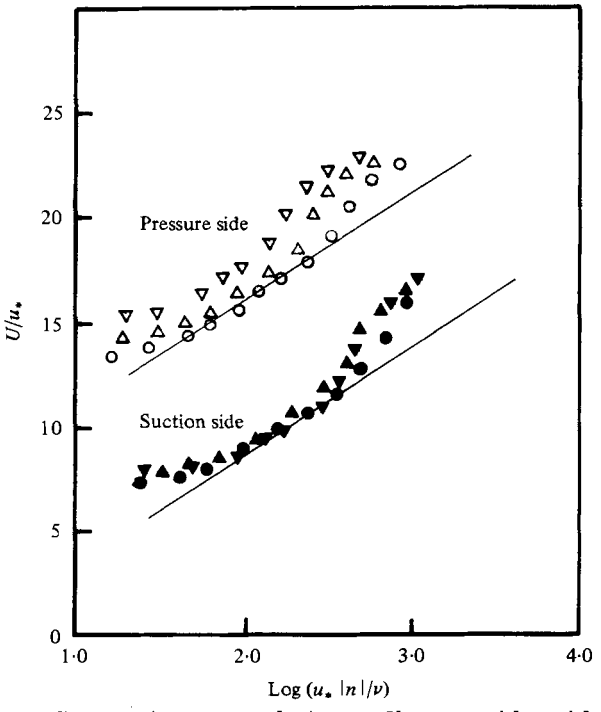

FIGURE 4. Streamwise mean velocity profile on semi-logarithmic scale at $s/C = 0$. ○, ●, $i = 3°$; △, ▲, $i = 6°$; ▽, ▼, $i = 9°$.

suction side of the airfoil. At the region very close to the trailing edge of the airfoil, the mean velocity profiles show the characteristics of a boundary layer, with substantial asymmetry for all three incidence angles. Due to the unfavourable pressure gradient, the boundary layer is thicker in the suction side than that in the pressure side near the trailing edge of the airfoil. For all three incidence angles, the velocity profiles show that the boundary layer is not separated and no recirculating zone is involved for the present experiment. The mean velocity profiles become almost symmetric after one chord downstream. It is also evident that the decay rate slows down with an increase in the incidence.

In figure 4, the mean-velocity profiles at the trailing edge are plotted in 'law of the wall' co-ordinates. The friction velocity (u_*) in this figure was estimated from the velocity profile in the wake. The solid line shows velocity defect laws in the inertial sublayer. The experimental data are in good agreement with these velocity defect laws in the inertial sublayer and the outer region, although some scattering is observed towards the wake centre region. The data illustrated in this figure demonstrate that the flow structure at the very near wake is similar to that of a typical boundary layer. Also, the existence of a flow region, where the logarithmic velocity profile prevails, is clearly shown.

As presented in figure 5, an attempt is made to check the similarity in velocity profiles by reducing the mean-velocity profile to a single curve through the use of suitable velocity and length scales. The difference between the maximum and minimum streamwise velocities across the wake was used as the velocity scale ($U_\infty - U_c$). U_c is the streamwise velocity at the wake centre. Two length scales, which are distances

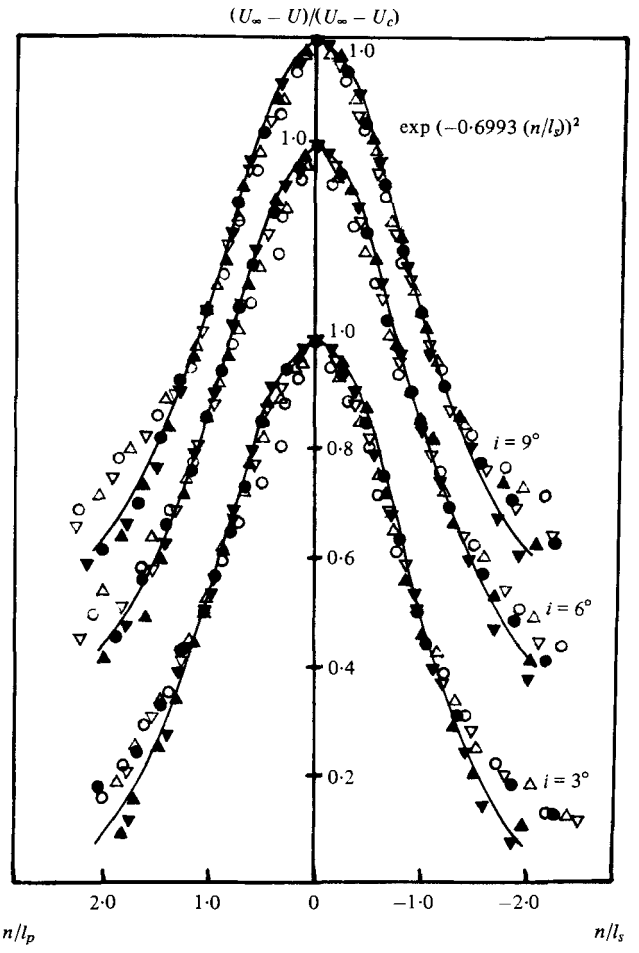

FIGURE 5. Similarity for mean velocity profile. ○, $s/C = 0$; △, $s/C = 0{\cdot}032$; ▽, $s/C = 0{\cdot}16$; ●, $s/C = 0{\cdot}28$; ▲, $s/C = 0{\cdot}94$; ▼, $s/C = 1{\cdot}5$.

from the wake centre to the points where the streamwise velocity defect is half of the maximum velocity defect on the pressure and suction sides, respectively, were used. These are denoted as l_p and l_s, respectively, in figure 5. The figure shows that the similarity in velocity profile with the proposed velocity and length scales exist except in the very-near-wake region ($s/C \leqslant 0{\cdot}032$). In the very near wake, the characteristic length and velocity scales are inner scales, and a similarity rule based on outer scales cannot be used. All the similarity profiles in figure 5 seem to follow the Gauss function $\exp[-0{\cdot}6993(\eta/l_s)^2]$, except the very near wake.

The decay of the wake centre-line velocity defect $(U_\infty - U_c)$ is presented for three incidence angles and compared with numerical prediction in figure 6. This shows that the wake decay rate is directly correlated to the incidence angles. At the very-near-wake region, the defect is almost the same for all three incidence angles. However, the decay rate is faster at lower incidence angles in the near-wake region. Beyond $s/C = 1{\cdot}0$, the decay rate slows down for lower incidence angles compared to that of higher incidence angles. Consequently, almost the same wake defect is observed at the far wake region, and the history effect becomes smaller in that region. The experimental data

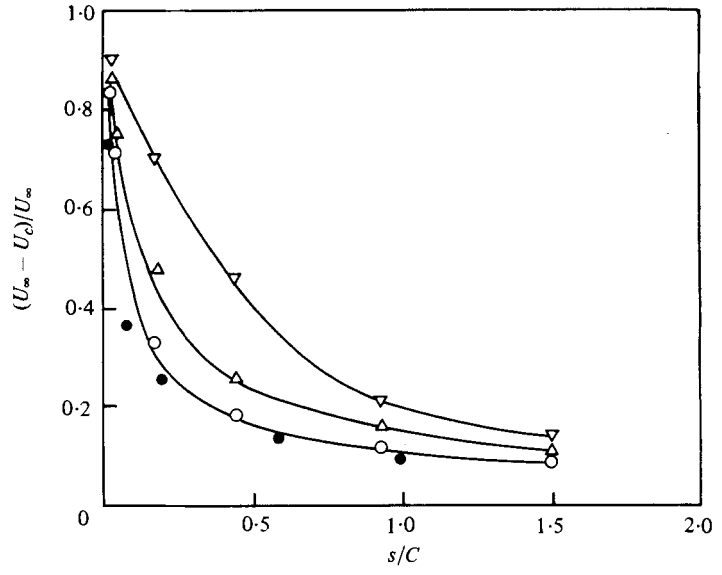

FIGURE 6. Decay of wake centre-line velocity defect. ○, $i = 3°$; △, $i = 6°$; ▽, $i = 9°$; ●, flat plate wake by Chevray & Kovasznay (1969); —, predictions for asymmetric wakes.

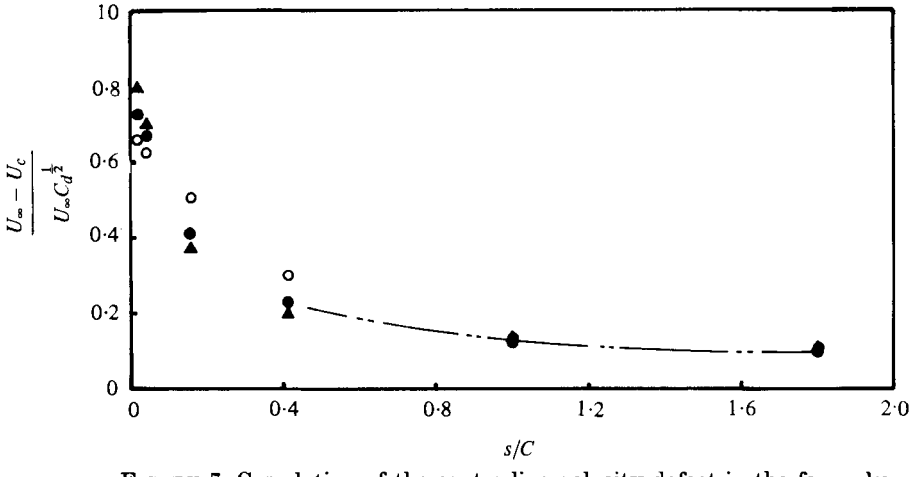

FIGURE 7. Correlation of the centre-line velocity defect in the far wake. ▲, $i = 3°$; ●, $i = 6°$; ○, $i = 9°$; —··—, equation (13) with $\beta = 0{\cdot}18$.

provided by Chevray & Kovasznay (1969) are also compared in figure 6. The velocity recovery at the wake centre occurs much earlier for lower incidence angles (50 % of free-stream velocity is recorded for $i = 3°$, while only 20 % is recorded for $i = 9°$ at $s/C = 0{\cdot}1$).

Figure 7 shows an attempt to reduce various wake-decay plots to a single curve using outer scales. The correlation curve for the far wake in this figure is from the analytical solution by Schlichting (1968), given in (13). The values of C_d used in figure 7 were evaluated from the momentum thicknesses in the wake and are consistent with experimentally obtained values by Abbott & Doenhoff (1958). The values of lift coefficient, C_l, and drag coefficient, C_d, are given in table 1. As expected, figure 7 demonstrates that the decay law of the wake defect based on the outer scale does not

	Incidence angle (i)		
	3°	6°	9°
C_l	0·338	0·621	0·901
C_d	0·011	0·014	0·019

TABLE 1. Section lift coefficient (C_l) and drag coefficient (C_d) for three incidence angles for NASA 0012 airfoil use.

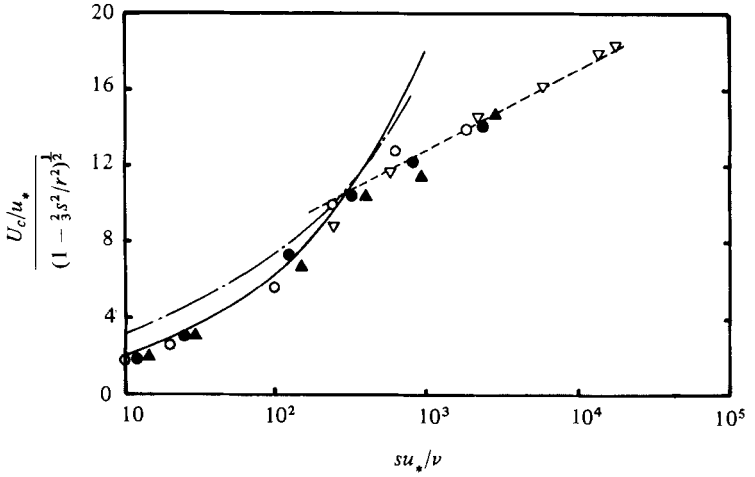

FIGURE 8. Centre-line velocity in the near wake of a single airfoil. ▽, flat plate wake by Chevray & Kovasznay (1969); —, equation (10) with $D_p = 0{\cdot}0$; – – –, equation (12) with $k' = 0{\cdot}41$ and $B' = 5{\cdot}0$; —· —, Goldstein's (1930) near-wake solution. Data: ▲, $i = 3°$; ●, $i = 6°$; ○, $i = 9°$.

describe very near wake and near wake. At very near wake and near wake, the wake centre region is dominated by the viscous sublayer and inertial sublayer. Therefore, the inner scale should be used for any successful correlation at these regions. The experimental data in the very near and near wakes, as presented in figure 8, are compared with the correlation based on inner scale equations (10) and (12). Also, Goldstein's (1930) solution for the fully laminar flow is compared with the experimental data. The radius of curvature was estimated from the wake centre-line trajectory. The reasonably good agreement between experimental data and correlation equations (10) and (12) shows that the decay of the mean velocity defect at the very near and near wakes can be properly correlated through the decay laws based on inner scales of the wake. As was shown in figures 7 and 8, any decay law based on single length scales cannot be used for the description of the entire wake region, and different decay laws based on the locally prevailing length scales should be used for successful correlation.

The variations of momentum thickness (θ) for three incidence angles are shown compared with numerical prediction in figure 9. Also shown are variations of the shape factor (H), which is the ratio of displacement thickness (δ^*) to momentum thickness. The displacement thickness and momentum thickness are defined as follows:

$$\delta^* = \int_{-\infty}^{\infty} \left(1 - \frac{U}{U_\infty}\right) dn, \quad \theta = \int_{-\infty}^{\infty} \left(1 - \frac{U}{U_\infty}\right) \frac{U}{U_\infty} dn. \qquad (24), (25)$$

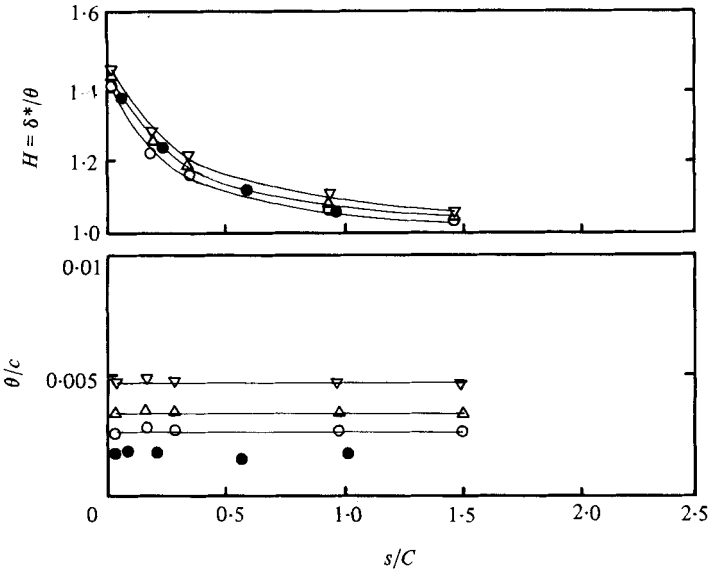

FIGURE 9. Variation of momentum thickness and shape factor. —, prediction for asymmetric wake. ○, $i = 3°$; △, $i = 6°$; ▽, $i = 9°$; ●, flat plate wake by Chevray & Kovasznay (1969).

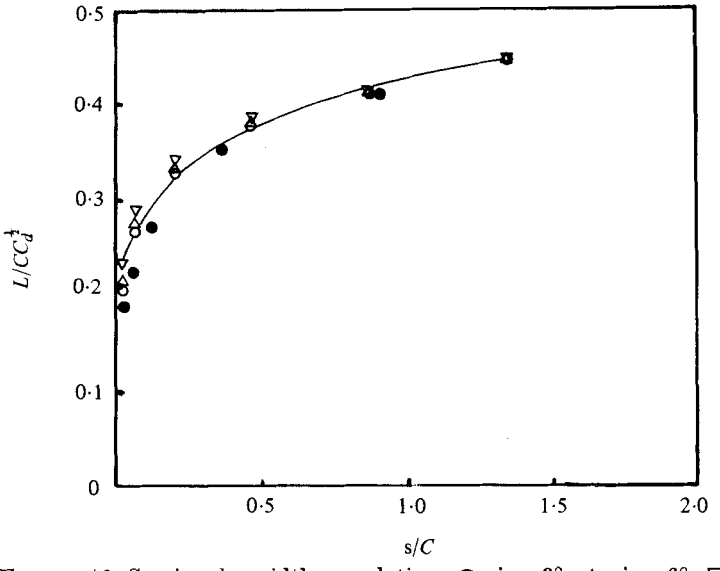

FIGURE 10. Semi-wake width correlation. ○, $i = 3°$; △, $i = 6°$; ▽, $i = 9°$; ●, flat plate wake by Chevray & Kovasznay (1969); —, equation (26).

As expected, the momentum thickness in the wake increases with the blade loading. Unlike the cascade wake (Raj & Lakshminarayana 1973) and the rotor blade wake (Reynolds, Lakshminarayana & Ravindranath 1979), the momentum thickness is almost constant downstream of the trailing edge of the airfoil. The shape factor converges to the value 1 downstreamwise regardless of loading on the airfoil. The shape factor value of 1·4 near the trailing edge indicates that the flow is not separated in this region.

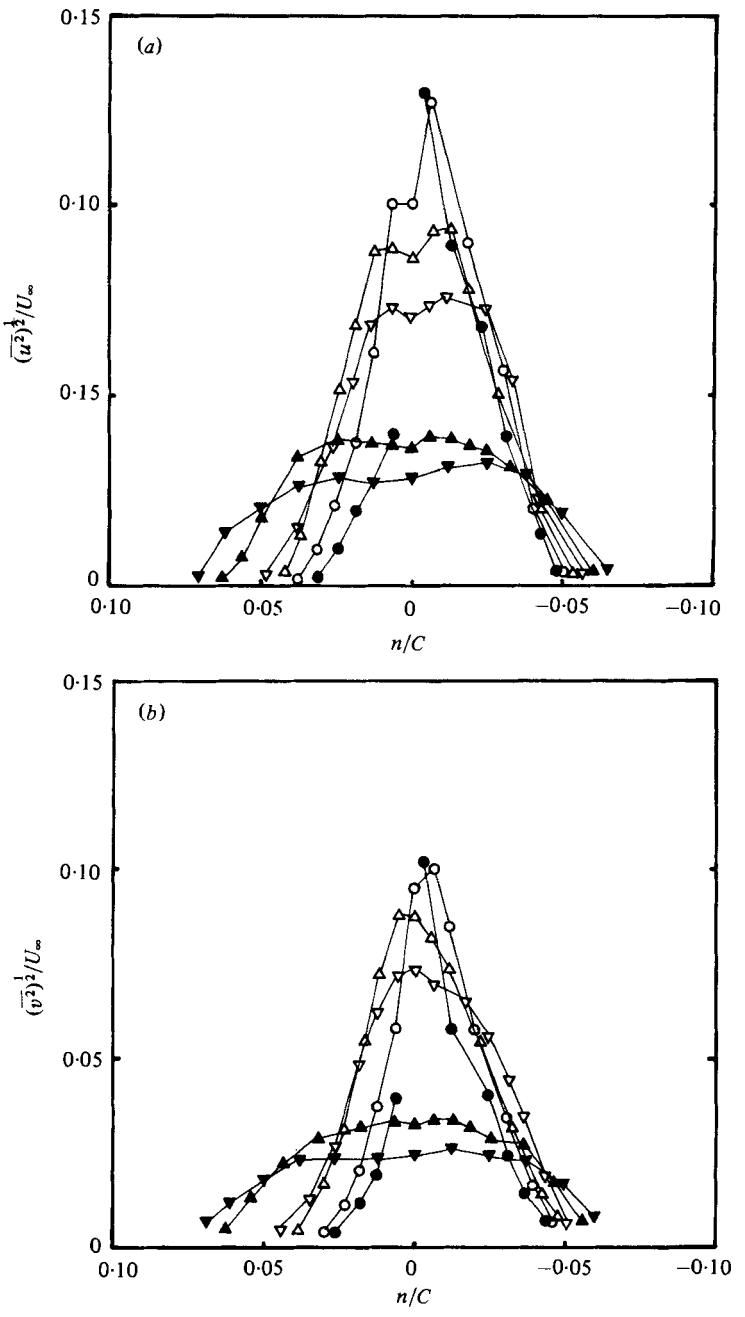

Caption for figures 11 (*a*, *b*) on p. 266.

The variation of semi-wake width is shown in figure 10. Semi-wake width (L) is defined as the width of the wake where the total mean velocity defect is one-half of the velocity defect at the wake centre. The widths on the pressure side (l_p) and suction side (l_s) are added to get the value of L. Experimental data show that the wake width increases with the higher blade loading, which is consistent with the increase of the boundary-layer thickness with higher loading. In figure 10, the variation of semi-wake

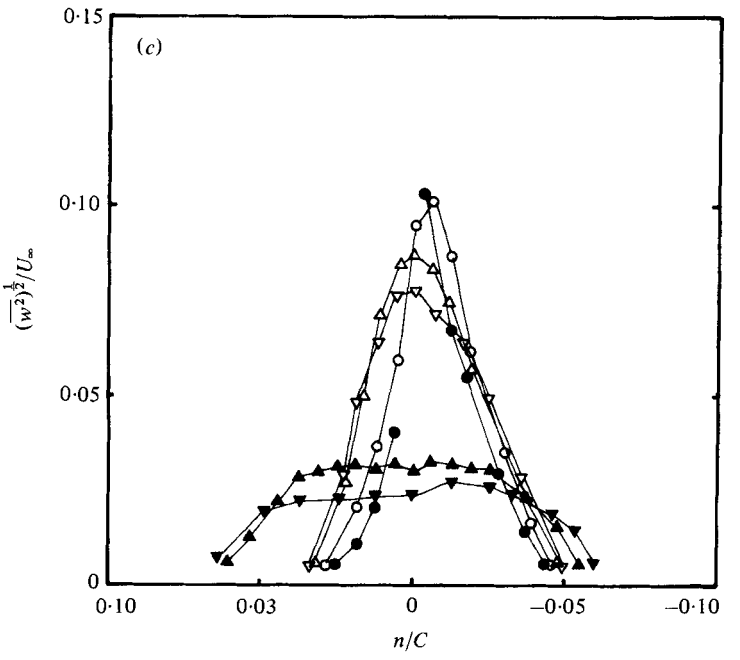

FIGURE 11. (*a*) Streamwise, (*b*) normal and (*c*) spanwise turbulence intensity distributions for $i = 3°$. ●, $s/C = 0$; ○, $s/C = 0{\cdot}032$; △, $s/C = 0{\cdot}16$; ▽, $s/C = 0{\cdot}28$; ▲, $s/C = 0{\cdot}94$; ▼, $s/C = 1{\cdot}5$.

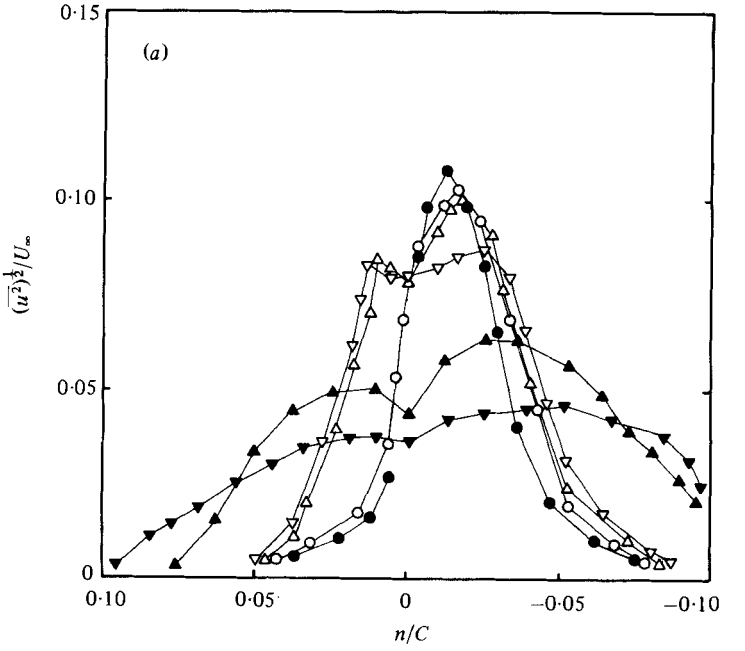

Caption for figure 12 (*a*) on p. 267.

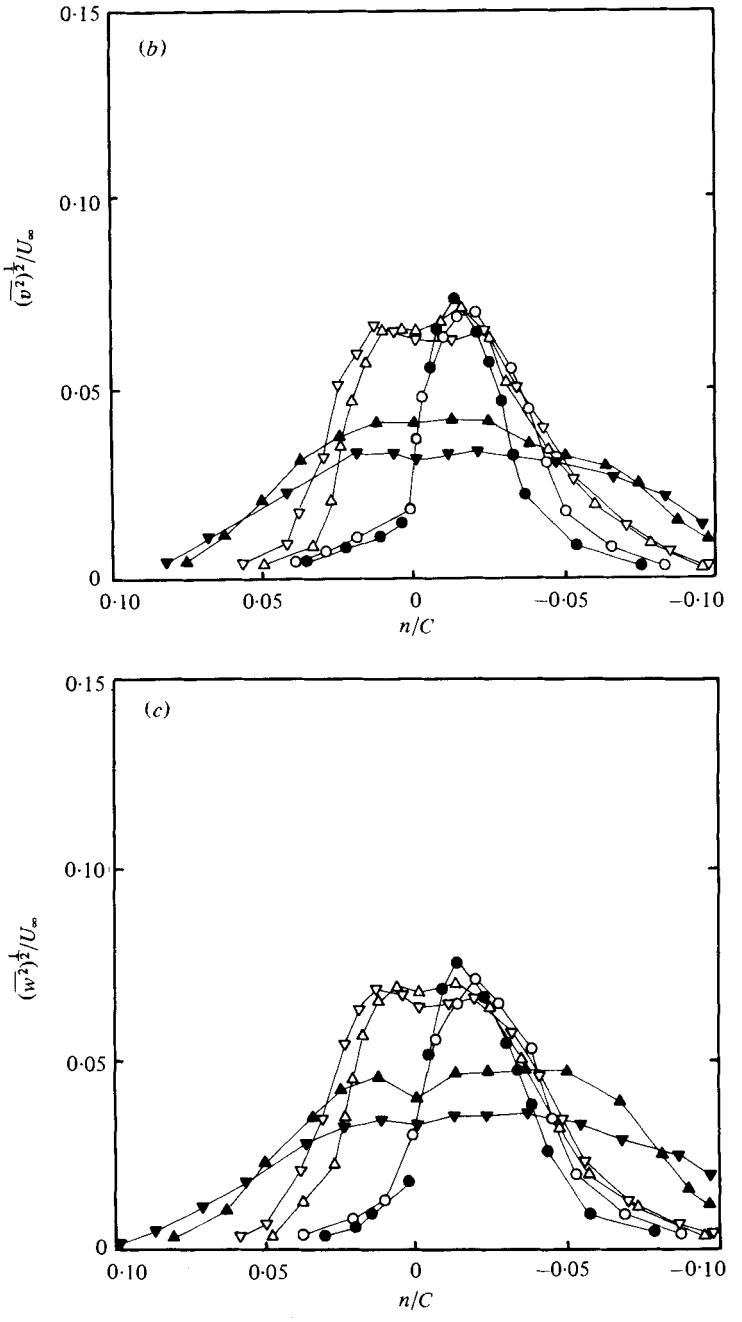

FIGURE 12. (*a*) Streamwise, (*b*) normal and (*c*) spanwise turbulence intensity distributions for $i = 6°$. ●, $s/C = 0$; ○, $s/C = 0{\cdot}032$; △, $s/C = 0{\cdot}16$; ▽, $s/C = 0{\cdot}28$; ▲, $s/C = 0{\cdot}94$; ▼, $s/C = 1{\cdot}5$.

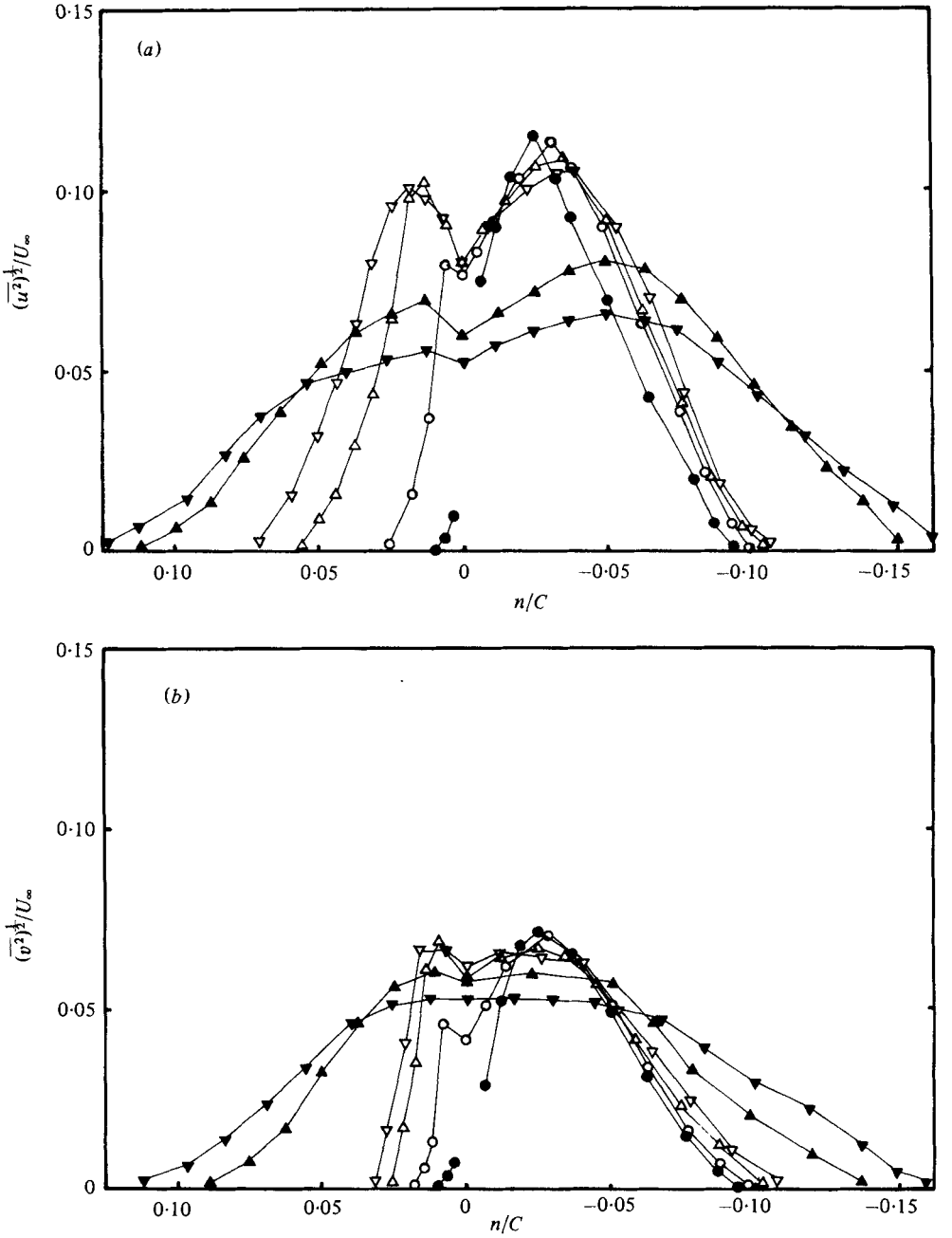

Caption for figures 13 (*a*, *b*) on p. 269.

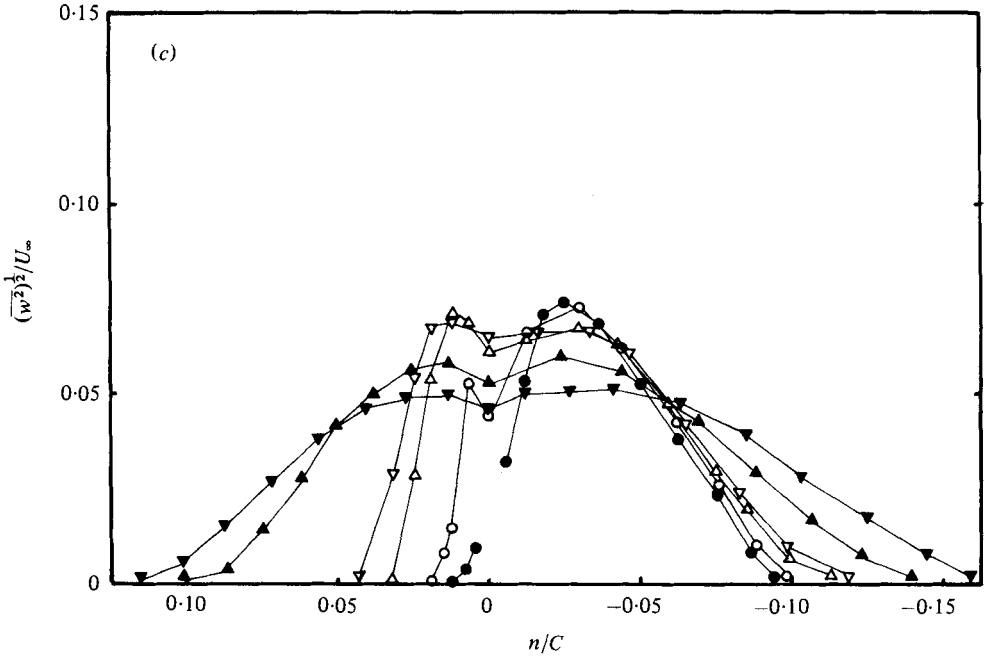

FIGURE 13. (*a*) Streamwise, (*b*) normal and (*c*) spanwise turbulence intensity distributions for $i = 9°$. ●, $s/C = 0$; ○, $s/C = 0{\cdot}032$; △, $s/C = 0{\cdot}16$; ▽, $s/C = 0{\cdot}28$; ▲, $s/C = 0{\cdot}94$; ▼, $s/C = 1{\cdot}5$.

width is correlated using $C_d^{\frac{1}{2}}$. It is interesting to note that most of the data points can be approximately represented with the following single correlation:

$$\frac{L}{C\sqrt{C_d}} = D_1\left(\frac{s}{C} - \frac{s_0}{C}\right)^{\frac{1}{2}}, \tag{26}$$

where D_1 is constant and s_0/C represents virtual origin of the wake. The values of D_1 and s_0/C are 0·29 and 0·36, respectively. Figure 10 shows that the semi-wake width correlates well in the far wake, although considerable scatters are observed in the very near wake. The correlation in this figure confirms that the effect of loading can be well represented with C_d at far downstream, but C_d cannot be used for the loading effect at very near wake.

5.2. *Turbulence properties*

The relative turbulence intensity distributions across the wake at several streamwise locations are shown in figures 11, 12 and 13 for 3°, 6° and 9° incidences, respectively. The intensity values are non-dimensionalized with free-stream velocity. For all three incidence angles, the turbulence intensity level is lower on the pressure side than on the suction side in the very-near-wake region. The fact that the mean velocity gradient is steeper in the pressure side than in the suction side indicates that the turbulence kinetic energy is not linearly related to the mean shear rate, and that the simple mixing length or eddy viscosity cannot be used for the turbulence closure in this region. The dip near the wake centre in the turbulence intensity is observed for all three incidence angles in the near- and far-wake regions. The dip in the turbulence-intensity profile disappears faster for the normal intensity component than for the

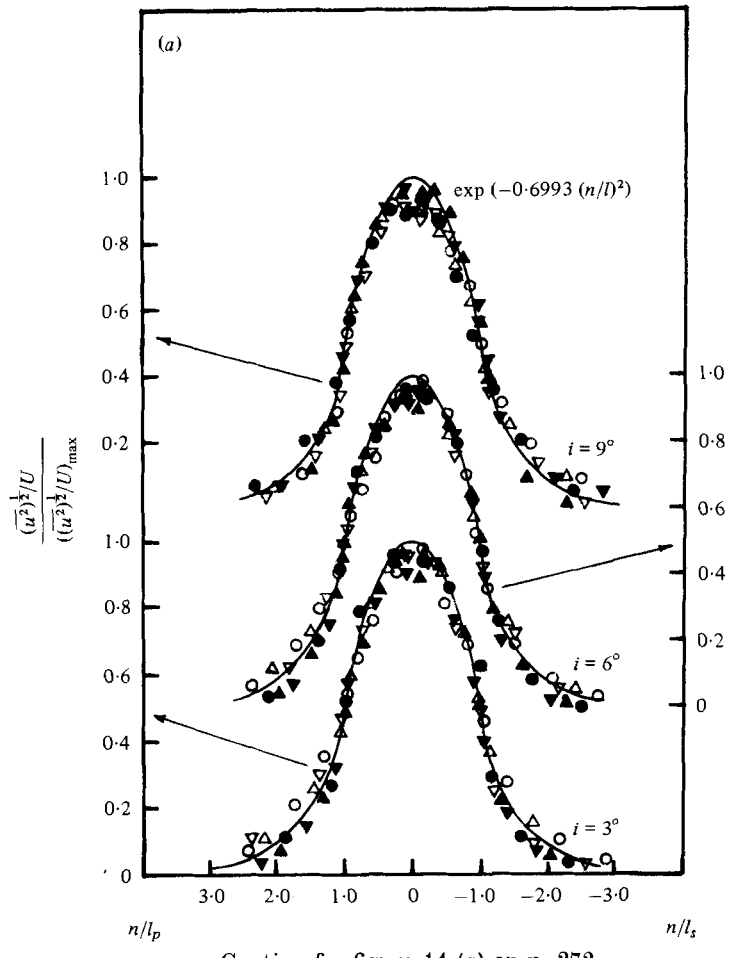

Caption for figure 14 (*a*) on p. 272.

other two components, as usually observed in the far wake of a cylinder. In the very near wake, the turbulence-intensity level is low on the pressure side and high on the suction side across the wake centre-line, and the dip in the profile is hardly observed. In the very near wake, the wake width is extremely thin and the measuring stations across the wake were not close enough to detect the dip. The width of the dip is related to the boundary-layer thickness, and is also different between intensity components. The profile of turbulence intensity across the wake is highly asymmetric at the very near wake and near wake, but becomes more symmetric downstream. The symmetric profile is achieved more slowly for higher incidence angles. The intensity profile does not have a dip at the wake centre in the very near wake; however, in the near wake, the turbulence-intensity level increases fast enough to form a dip. Then the profile changes the same way that a symmetric wake decays.

The maximum turbulence intensity occurs very close to the wake centre-line at near wake. However, far downstream of the airfoil, maximum turbulence intensity occurs away from the centre-line due to the spread of the wake. The streamwise turbulence-intensity component is much higher than the normal and spanwise intensity components at very near wake, but the difference in magnitude disappears far

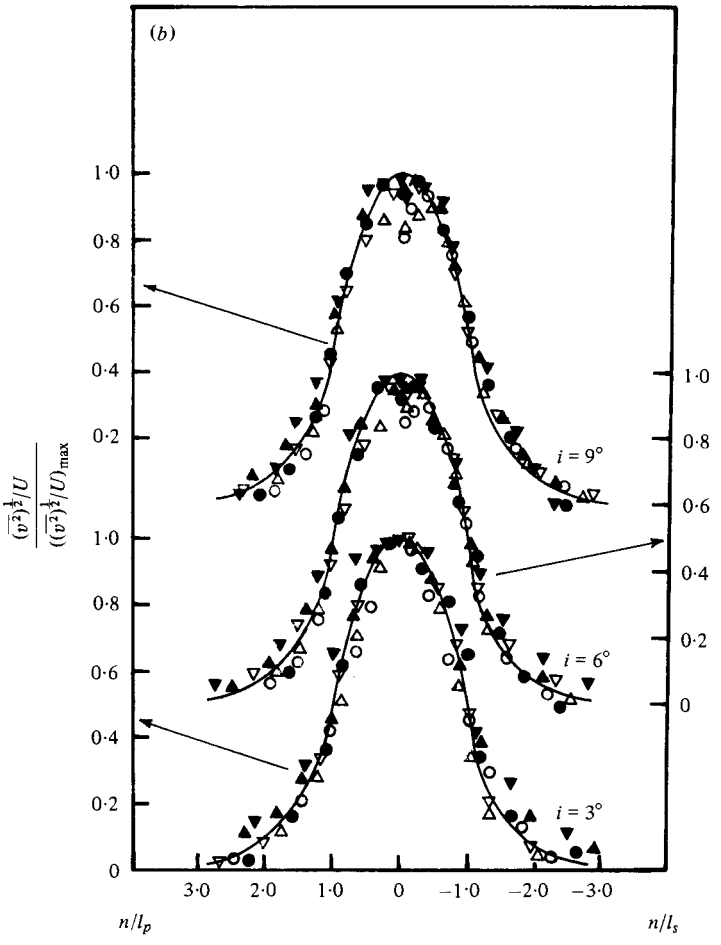

Caption for figure 14 (*b*) on p. 272.

downstream due to the more isotropic turbulence structure. The maximum values of turbulence intensity at the very near wake are almost the same for all three incidence angles. Throughout all of the wake regions, the relative magnitudes of the three intensity components are $(\overline{u^2})^{\frac{1}{2}}/U_\infty > (\overline{w^2})^{\frac{1}{2}}/U_\infty \geqslant (\overline{v^2})^{\frac{1}{2}}/U_\infty$.

The similarity rule was examined for turbulence-intensity profiles, which are shown plotted in figures 14(*a*, *b*, *c*) for the streamwise, normal and spanwise directions, respectively. In these plots, the turbulence intensity was normalized with the maximum turbulence intensity. In situations where a dip was noticed at the wake centre, an extrapolated peak intensity near the wake centre was chosen. Also, free-stream turbulence intensity was subtracted from the local values. The distances from the wake centre-line to the locations where the local turbulence intensity is half of the maximum turbulence intensity were chosen as the characteristic length scales l_p and l_s for the pressure and suction sides, respectively. Similarity profiles seem to follow the Gauss distribution ($\exp[-0{\cdot}6933(n/l_s)^2]$ or $\exp[-0{\cdot}6933(n/l_p)^2]$). However, a large discrepancy is observed in the outer region of the wake as well as at very near wake.

The decay rate of the maximum turbulence intensity downstream of the trailing

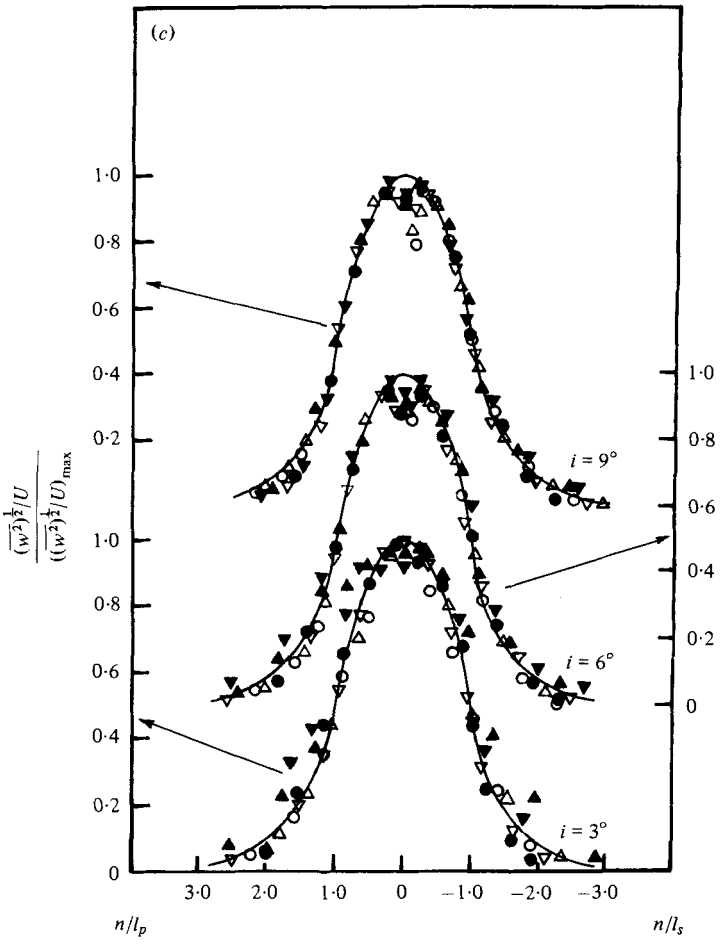

FIGURE 14. Similarity in the (*a*) streamwise, (*b*) normal and (*c*) spanwise turbulence intensity profiles. ○, $s/C = 0$; △, $s/C = 0{\cdot}032$; ▽, $s/C = 0{\cdot}16$; ●, $s/C = 0{\cdot}28$; ▲, $s/C = 0{\cdot}94$; ▼, $s/C = 1{\cdot}5$; —, exp $[-0{\cdot}6993(n/l)^2]$.

edge is shown in figure 15. The decay of the streamwise intensity component is faster than the normal and the spanwise intensity components at the near wake, and the three components decay at nearly the same rate far downstream and reach more isotropic conditions. The variations of the three maximum intensity components can be approximately represented by

$$((\overline{u^2})^{\frac{1}{2}}/U_\infty)_{\max}, \quad ((\overline{v^2})^{\frac{1}{2}}/U_\infty)_{\max}, \quad ((\overline{w^2})^{\frac{1}{2}}/U_\infty)_{\max} \times 100 = a_i(s/\theta_0 + s_0/\theta_0)^{b_i}, \quad (27)$$

where θ_0 is the momentum thickness at the trailing edge of the airfoil and a_i, b_i, s_0/θ_R are 21·3, −0·33 and 0·04 for the streamwise component; 19·2, −0·23 and 0·03 for the normal component; and 19·0, −0·22 and 0·03 for spanwise component. Equation (27) is also plotted in figure 15 as solid lines, and represents the experimental data quite well.

The streamwise shear stress distribution is shown in figures 16(*a*, *b*, *c*) for $i = 3°$, 6° and 9°, respectively. The shear stress is non-dimensionalized with free-stream streamwise mean velocity in these figures. The shear stress profiles are asymmetric

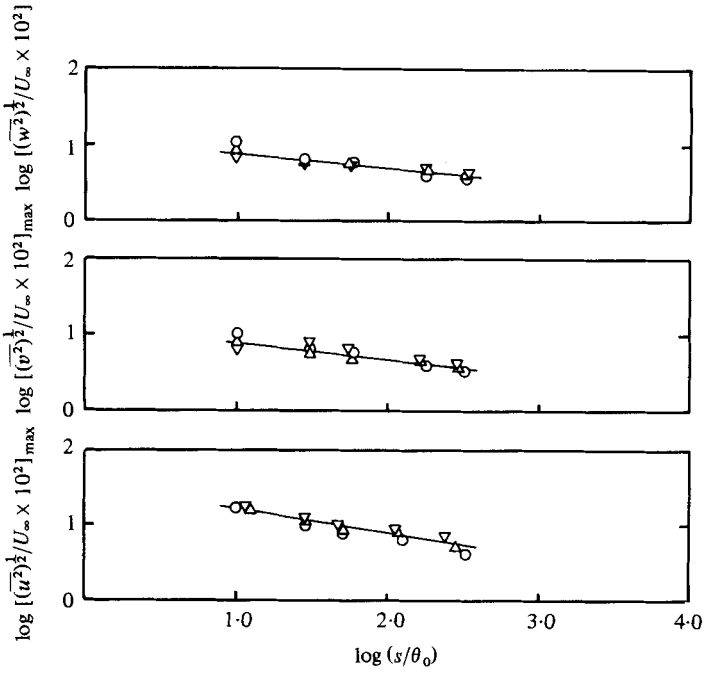

FIGURE 15. Decay of maximum turbulence intensity components. —, equation (27). ○, $i = 3°$; △, $i = 6°$; ▽, $i = 9°$.

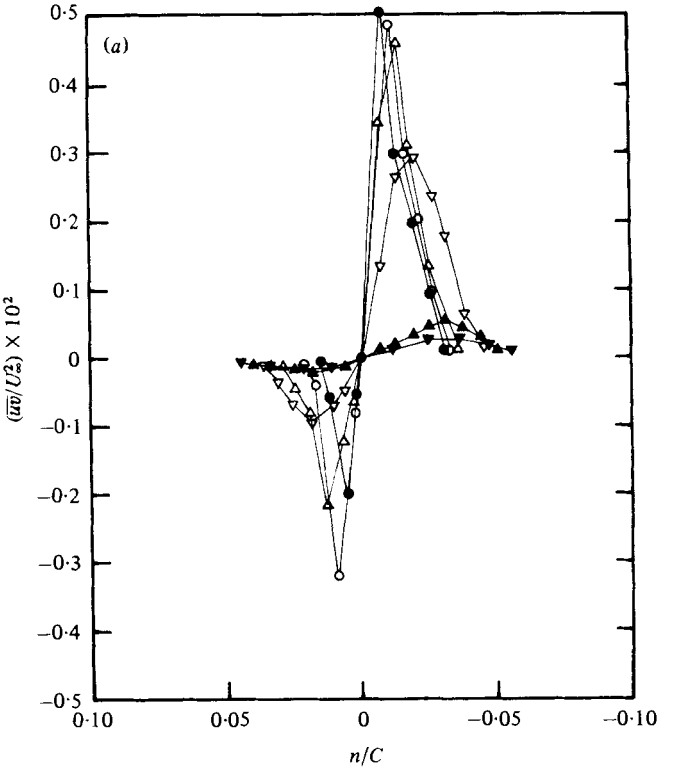

Caption for figure 16 (*a*) on p. 274.

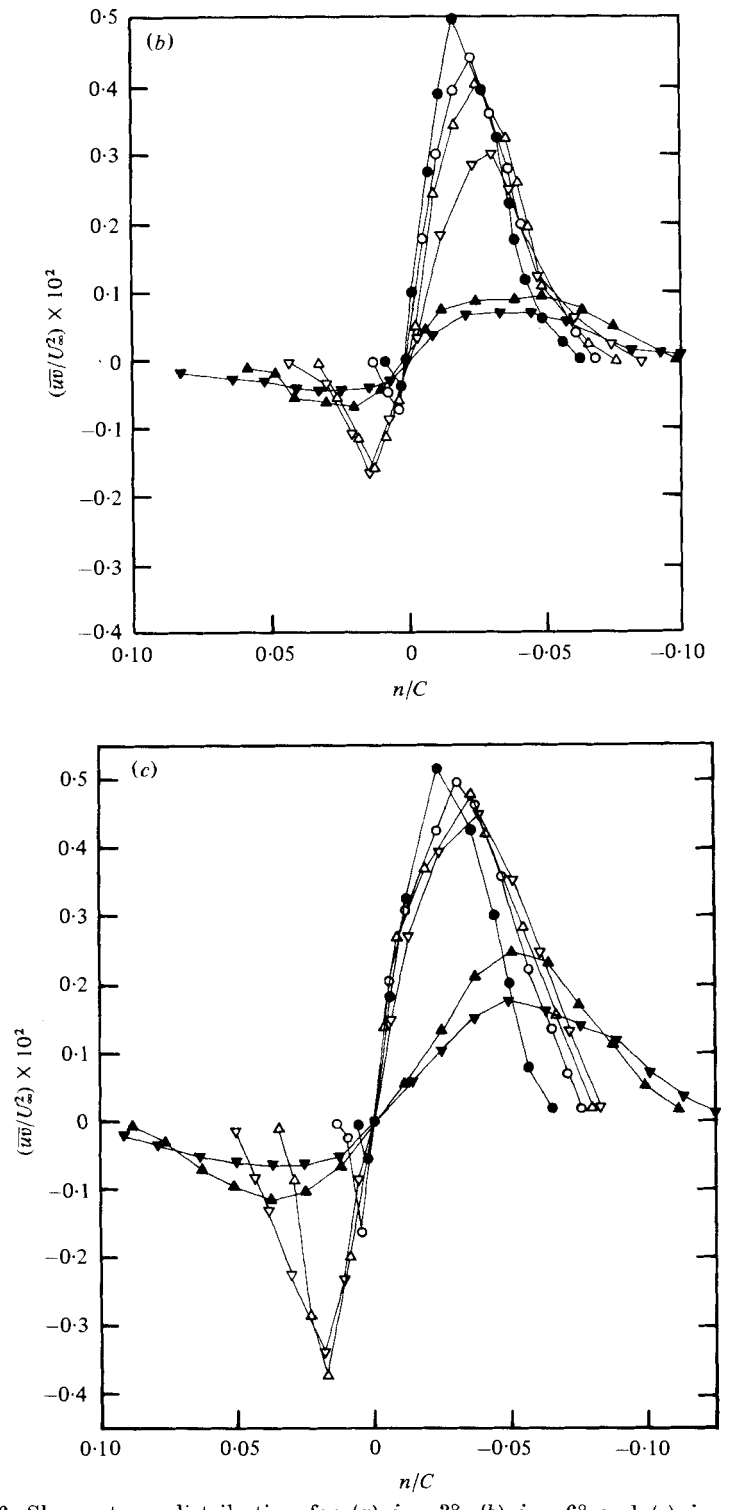

FIGURE 16. Shear stress distribution for (*a*) $i = 3°$, (*b*) $i = 6°$ and (*c*) $i = 9°$. ●, $s/C = 0$; ○, $s/C = 0{\cdot}032$; △, $s/C = 0{\cdot}16$; ▽, $s/C = 0{\cdot}28$; ▲, $s/C = 0{\cdot}94$; ▼, $s/C = 1{\cdot}5$.

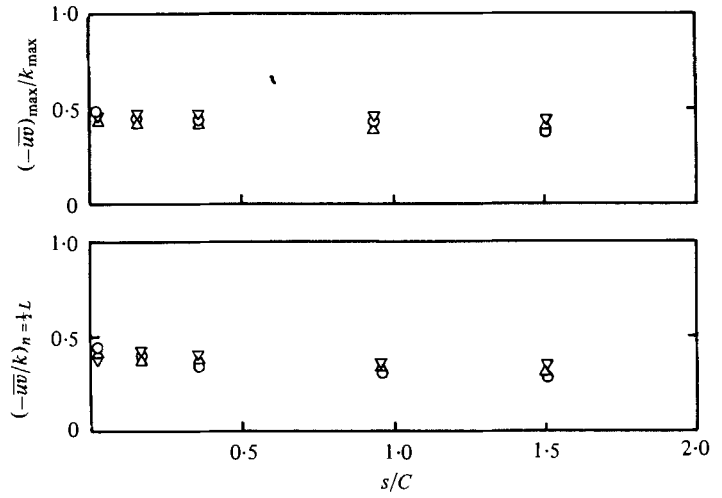

FIGURE 17. Ratio of maximum shear stress to maximum turbulence kinetic energy at half-wake width. ○, $i = 3°$; △, $i = 6°$; ▽, $i = 9°$.

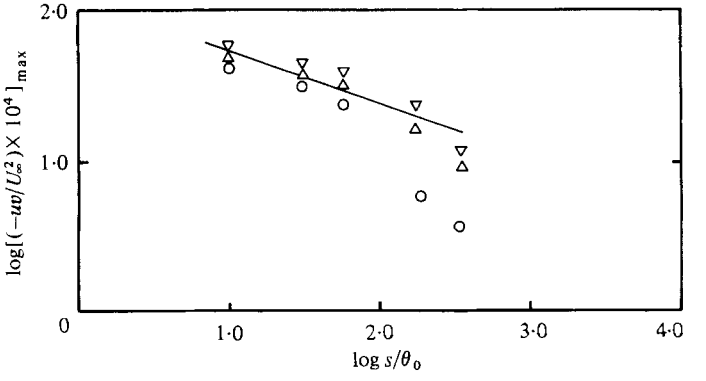

FIGURE 18. Decay of maximum shear stress. —, equation 28. ○, $i = 3°$; △, $i = 6°$; ▽, $i = 9°$.

at the near wake and become symmetric beyond one chord downstream. At the very near wake, the magnitude of the shear stress in the pressure side is smaller than that in the suction side of the airfoil, and the difference in the magnitudes of shear stresses becomes smaller downstream. As in the case of turbulence intensity, the maximum value of shear stress in the suction side does not vary according to the incidence angle, and is of the same order of magnitude as the wake of a flat plate (Chevray & Kovasznay 1969). The difference of magnitude of shear stresses between the suction side and pressure side of the airfoil as well as their absolute magnitude depend on the blade loading or incidence angle. This is because the streamline curvature in the wake is dependent on the incidence angle, and the turbulence diffusion is very sensitive to the streamline curvature. The shear stress changes its sign near the wake centre-line, but the zero shear stress does not always occur at the point of minimum mean velocity. The lower value of shear stress in the pressure side, where the mean-velocity gradient is much larger than that in the suction side, indicates that any eddy-viscosity or mixing-length model requires a proper modification for the asymmetric nature of the wake. The width

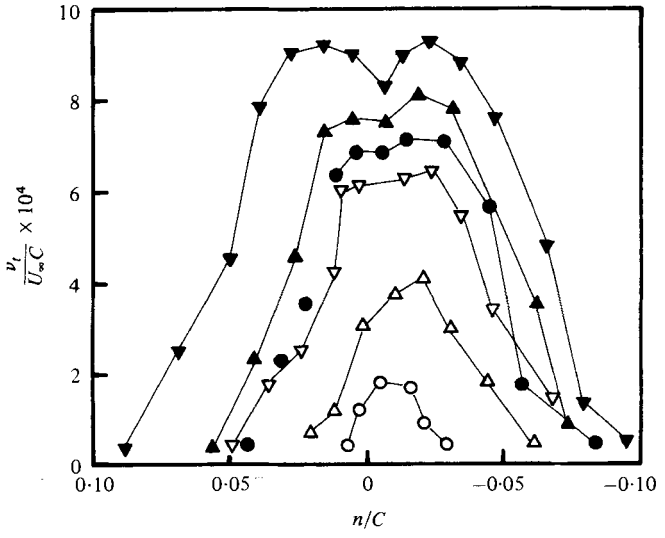

FIGURE 19. Eddy viscosity in the wake. ○, $s/C = 0$; △, $s/C = 0{\cdot}032$; ▽, $s/C = 0{\cdot}16$; ●, $s/C = 0{\cdot}28$; ▲, $s/C = 0{\cdot}94$; ▼, $s/C = 1{\cdot}5$.

between points where maximum shear stress occurs in the pressure and suction sides of the airfoil is narrower than that of turbulence intensity for all three incidence angles, as shown in figures 16(*a*, *b*, *c*).

According to previous experimental studies of symmetric turbulent wakes of a single airfoil or a flat plate (Klebanoff 1955; Chevray & Kovasznay 1969), the magnitude of shear stress is nearly equal to $0{\cdot}3k$ (k is turbulence kinetic energy). The present experimental results indicate that this relation is not quite valid for asymmetric turbulent wakes. Figure 17 shows the ratio of shear stress to turbulence kinetic energy at half of the wake width. The magnitude of this ratio varies from 0·4 in the trailing-edge region to 0·3 far downstream. Also shown in figure 17 is the variation of $(-\overline{uv})_{\max}/k_{\max}$ for three incidence angles, whose value also varies slightly from trailing region to far-wake region. The decay of maximum shear stress is shown in figure 18. The maximum shear-stress decay can be approximately represented by the following equation:

$$[(-\overline{uv})_{\max}/U_\infty^2] \times 10^4 = 121(s/\theta_0 + s_0/\theta_0)^{-0{\cdot}45}, \tag{28}$$

where s_0/θ_0 represents the virtual origin, and the value for this figure is 0·07.

The distribution of eddy viscosity ($\nu_t = -uv/(\partial U/\partial y)$) in the wake is shown in figure 19. The eddy viscosity was calculated using the experimental data. A fourth-order polynomial function was used to represent mean velocity profile in estimating eddy viscosity across the wake. Distribution is asymmetric in the near wake and becomes symmetric in the far wake. The large variation of the eddy viscosity across the wake as well as in the streamwise direction is clearly observable.

The turbulence data is examined for the property of self-preservation. The production of turbulence kinetic energy, neglecting the curvature and smaller terms in (15), is given by

$$-\overline{uv}\frac{\partial U}{\partial r} - (\overline{u^2} - \overline{v^2})\frac{\partial U}{\partial s}. \tag{29}$$

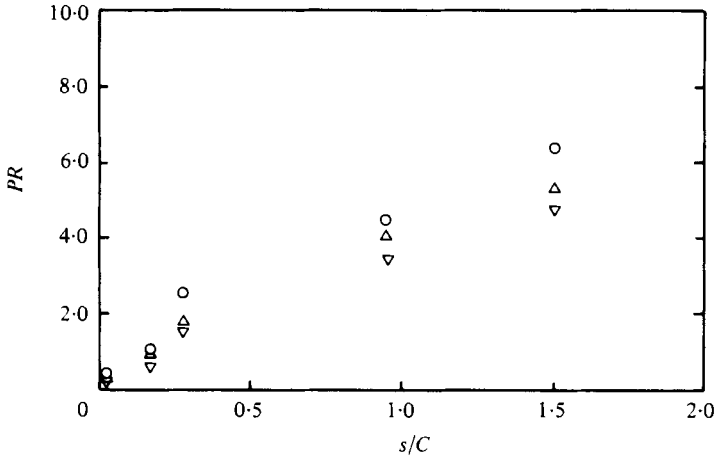

FIGURE 20. Variation of PR with downstream distance.
○, $i = 3°$; △, $i = 6°$; ▽, $i = 9°$.

The second term introduces non-self-preservation into the flow as it occurs in the description of an isotropic far wake. The first term is negligibly small in homogeneous, distorted turbulence. The production of turbulent energy depends on the shape of the body and the incidence angle in the present case. Reynolds (1962) deduced the following criteria for self-preservation, based on the above energy-production terms:

$$PR = \left[\frac{-\overline{uv}\,\partial U/\partial n}{(\overline{u^2}-\overline{v^2})\,\partial U/\partial s}\right]_{n=L}, \tag{30}$$

where L is half the wake width. Figure 20 shows the variation of PR for three incidence angles. The experimental data illustrated in figure 20 show that the self-preservation is attained more slowly when the loading on the blade is increased. For the present experiment, complete self-preservation is not attained for all three incidence angles (for complete self-preservation, $PR \geqslant 10$).

5.3. *Comparison between experimental data and numerical analysis*

The predicted results from the numerical analysis described in §3.3 are compared with the experimental data in figures 21–23. To represent the effect of streamline curvature on the development of an asymmetric wake with the presently adopted turbulence closure model, the source term described in (21) was used for the present prediction. Also, the results with the conventionally used source term (equation (20)) are compared at one streamwise location. As explained in §3.3, the governing equation was solved in elliptic form, and the necessary boundary conditions were obtained from the experimental data and the correlation law. The finite-difference equation was solved iteratively. The comparison of the mean velocity indicates that the profile and the decay of mean velocity are predicted accurately with the newly adopted source term in the energy dissipation equation. When the conventional source term (equation (20)) is used in the dissipation equation, some deviation in the velocity profile between theory and experimental data is observed in the pressure side, and the wake centreline velocity decay rate is predicted to be faster than is found in the actual experimental data. The present turbulence closure model with modified source term in the

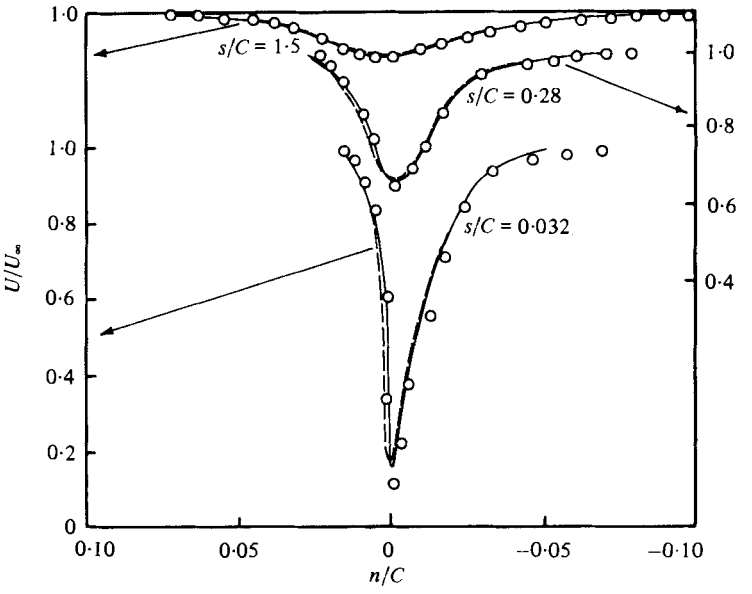

FIGURE 21. Comparison between predicted and measured streamwise mean velocity for $i = 6°$. ○, experiment; —, prediction with the dissipation equation (19) and (21); ----, prediction with the dissipation equation (19) and (20).

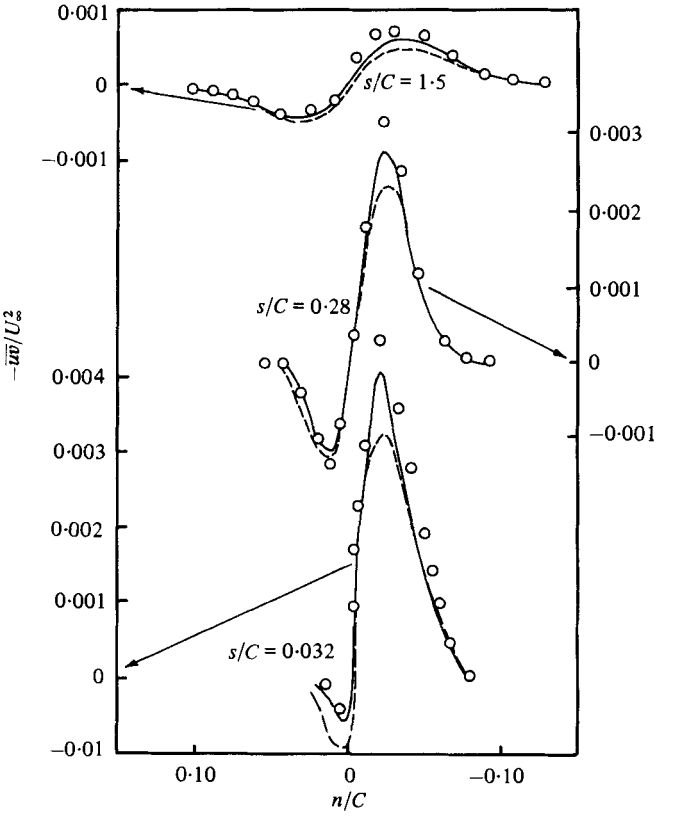

FIGURE 22. Comparison of the shear stress for $i = 6°$. ○, experiment; —, prediction with the dissipation equation (19) and (21); ----, prediction with the dissipation equation (19) and (20).

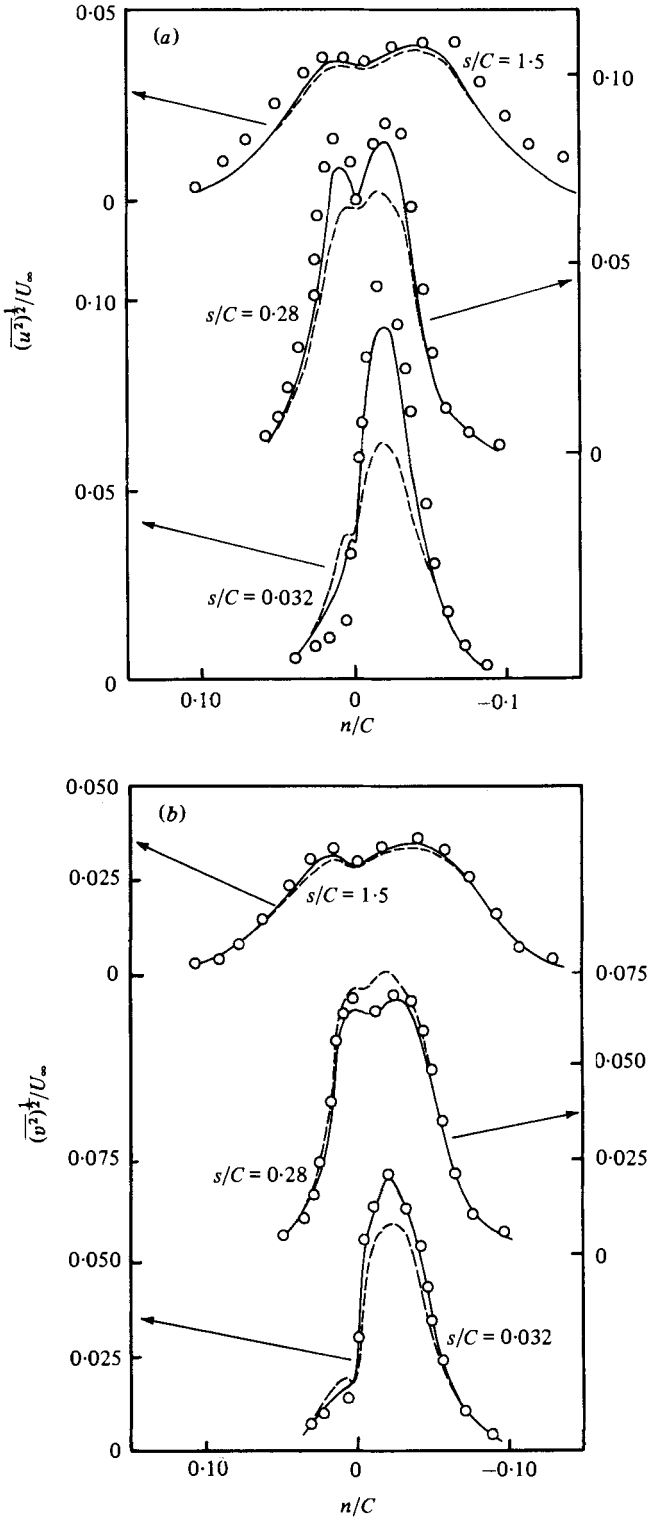

Caption for figures 23 (*a*, *b*) on p. 280.

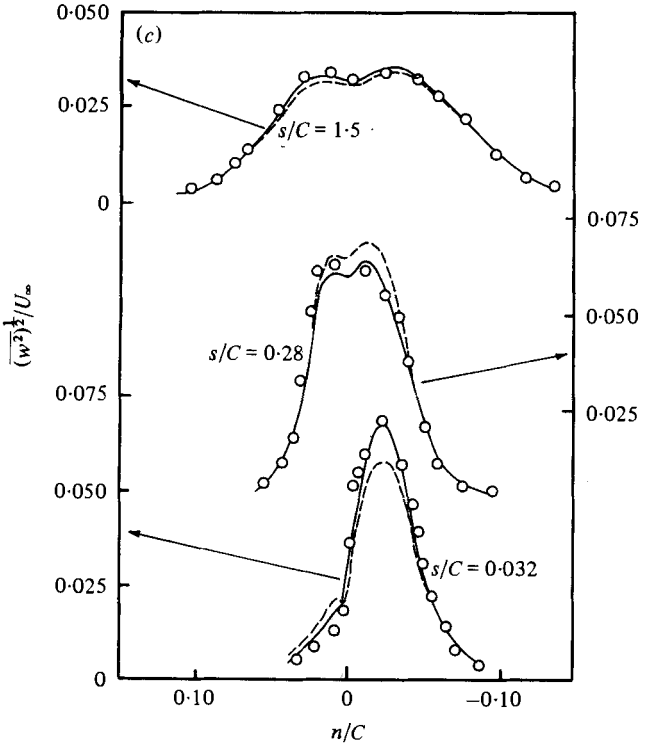

FIGURE 23. Comparison of the (*a*) streamwise, (*b*) normal and (*c*) spanwise turbulence intensity for $i = 6°$. ○, experiment; —, prediction with the dissipation equation (19) and (21); ----, prediction with the dissipation equation (19) and (20).

energy dissipation equation predicts the effects of streamline curvature accurately for the turbulence intensity (figures 23*a*, *b*, *c*) and Reynolds shear stress (figure 22). Here again, the prediction with the conventional source term in the energy dissipation equation shows considerable discrepancy from the experimental data. Both the turbulence intensity and Reynolds shear stress are overestimated in the pressure side and underestimated in the suction side of the airfoil with the conventional source term. Maximum difference between the predicted results and experimental data occurs for the streamwise turbulence-intensity component, especially at $s/C = 0{\cdot}28$, as shown in figure 23(*a*). As demonstrated through the comparison, the effect of streamline curvature on the development of the wake can be properly incorporated through modification of the energy dissipation equation. The numerical calculation required about 3 min of C.P.U. time using the I.B.M. 370/3033 with the nodes of 60×60.

6. Discussion and conclusions

The experimental data and numerical analysis reported in this paper indicate that the asymmetric wake of an isolated airfoil differs from the symmetric one in several respects. Some of the important conclusions are as follows.

(1) The decay rate of the mean velocity defect at the wake centre decreases when the incidence is increased.

(2) Similarity in mean velocity profile exists for all the incidences, except at the very near wake and at the wake centre regions. It seems to follow the Gaussian distribution when proper velocity and length scales are used.

(3) The conventional boundary layer characteristics, namely, increase in thickness in the suction side as compared to the pressure side at higher incidences, is observed in the wake.

(4) The asymmetric wake becomes nearly symmetric after one chord downstream of the trailing edge of the blade.

(5) The turbulence kinetic energy and shear stress increase in the suction side and decrease in the pressure side due to the effect of streamline curvature.

(6) The profiles of turbulence intensity show similarity when proper length and intensity scales are utilized. However, similarity is not evident in the wake centre and in the very near wake.

(7) The profile of turbulent shear stress distribution becomes more asymmetric at higher incidences and the profile changes to symmetric one more slowly than the turbulence intensity.

(8) The maximum turbulent shear stress decays faster than the maximum turbulence intensity for all the three incidence angles.

(9) The relationship between the turbulent kinetic energy and the shear stress observed for a symmetric wake is not valid for an asymmetric wake.

(10) The eddy viscosity calculated using the experimental values of the shear stress and the mean shear rate shows large variation in both streamwise and normal directions of the wake.

(11) The analysis based on outer scales of the wake do not correlate well with the wake data in the very near wake and the near wake. Analysis based on inner scales of the wake can be successfully used in correlating the experimental data in these regions.

(12) The streamline curvature, which arises from the non-zero incidence for the present study, substantially affects the profile of the mean velocity as well as the turbulence characteristics. The wake defect is almost doubled due to the curvature in the near wake when the incidence angle is changed from 3° to 9°.

The wake properties are predicted using the exact equations of motion and modelled equations of turbulence. To predict the asymmetric wake accurately, the effect of streamline curvature should be properly modelled in the turbulence closure scheme. The effect of streamline curvature cannot be properly accounted for when the production of turbulent kinetic energy is used as a source term in the energy dissipation equation. When a more rationally derived source term that does not include the mean shear rate is utilized, better agreement between theory and experiment is obtained and the effect of streamline curvature is properly accounted for.

This work was supported by the U.S. National Aeronautics and Space Administration, through the grant NSG 3012, with L. Shaw as the technical monitor.

REFERENCES

ABBOTT, I. H. & DOENHOFF, A. E. 1958 *Theory of Wing Sections*. Dover.
ALBER, I. E. 1979 *A.I.A.A. J.* **18**, 1044–1051.
BRADSHAW, P. 1973 *AGARDograph* no. 169.
CHEVRAY, R. & KOVASZNAY, S. G. 1969 *A.I.A.A. J.* **7**, 1641.
COLES, D. 1956 *J. Fluid Mech.* **1**, 191.
GOLDSTEIN, S. 1930 *Proc. Camb. Phil. Soc.* **26**, 3.
HAH, C. 1980 Ph.D. thesis, Dept. of Aerospace Engng, The Pennsylvania State University.
HAH, C. & LAKSHMINARAYANA, B. 1980*a* *A.I.A.A. J.* **18**, 1196.
HAH, C. & LAKSHMINARAYANA, B. 1980*b* *J. Fluids Engng* **102**, 462.
KLEBANOFF, P. S. 1955 *N.A.C.A. Rep.* no. 1247.
POPE, S. B. & WHITELAW, J. H. 1976 *J. Fluid Mech.* **73**, 9.
PRESTON, J. H. & SWEETING, N. E. 1943 *Aero. Res. Counc. R. & M.* no. 1998.
PRESTON, J. H., SWEETING, W. E. & COX, D. K. 1945 *Aero. Res. Counc. R. & M.* no. 2013.
RAJ, R. & LAKSHMINARAYANA, B. 1973 *J. Fluid Mech.* **61**, 707.
REYNOLDS, A. J. 1962 *J. Fluid Mech.* **13**, 333.
REYNOLDS, B., LAKSHMINARAYANA, B. & RAVINDRANATH, A. 1979 *A.I.A.A. J.* **17**, 9.
SCHLICHTING, H. 1968 *Boundary Layer Theory*. McGraw-Hill.
SILVERSTEIN, A., KATZOFF, S. & BULLIVANT, W. 1939 *N.A.C.A. Rep.* no. 651.